

Manuscript version: Author's Accepted Manuscript

The version presented in WRAP is the author's accepted manuscript and may differ from the published version or Version of Record.

Persistent WRAP URL:

<http://wrap.warwick.ac.uk/171363>

How to cite:

Please refer to published version for the most recent bibliographic citation information. If a published version is known of, the repository item page linked to above, will contain details on accessing it.

Copyright and reuse:

The Warwick Research Archive Portal (WRAP) makes this work by researchers of the University of Warwick available open access under the following conditions.

Copyright © and all moral rights to the version of the paper presented here belong to the individual author(s) and/or other copyright owners. To the extent reasonable and practicable the material made available in WRAP has been checked for eligibility before being made available.

Copies of full items can be used for personal research or study, educational, or not-for-profit purposes without prior permission or charge. Provided that the authors, title and full bibliographic details are credited, a hyperlink and/or URL is given for the original metadata page and the content is not changed in any way.

Publisher's statement:

Please refer to the repository item page, publisher's statement section, for further information.

For more information, please contact the WRAP Team at: wrap@warwick.ac.uk.

**Green fabrication of anti-friction slippery liquid-infused metallic surface
with sub-millimeter-scale asymmetric bump arrays and its application**

Zhongxu Lian^{a,b}, Yi Cheng^a, Jinkai Xu^{a*}, Jinlong Xu^a, Wanfei Ren^a, Yanling Tian^b, Huadong
Yu^a

*^aMinistry of Education Key Laboratory for Cross-Scale Micro and Nano Manufacturing,
Changchun University of Science and Technology, Changchun 130022, China*

^bSchool of Engineering, University of Warwick, Coventry CV4 7DL, UK

*Corresponding author.

E-mail address: xujinkai2000@163.com.cn.

Abstract: In this work, we present a simple technique for green fabrication of slippery liquid-infused surface (SLIS) with anti-friction property on various metallic substrates using wire electrical discharge machining. Micro-crater structures were successfully obtained, and the surface had excellent liquid-repellent property after modification and infusion of silicone oil. A wide range of liquids including water, juice, coffee, tea, vinegar, albumin, glycerol, and ketchup could easily slid down the surface tilted at an angle of 10° without leaving any trace. The influences of the number of cutting step on the morphology and wettability of the surface were studied comprehensively. Further, the tribological properties of the surface were analyzed and the results showed that the SLIS had a decrease of 73.2% in friction coefficient as compared to that of the smooth surface. By studying the morphology of the worn surfaces, it is found that the SLIS had slight abrasive wear behavior. To demonstrate the precision processing ability of this technology, we fabricated slippery sub-millimeter-scale asymmetric bump arrays, and the experiment results showed that the asymmetric bump arrays had excellent water harvesting ability at low temperatures. This kind of environment-friendly precision machining technology will promote the practical applications of metallic functional materials.

Keywords: green fabrication, wire electrical discharge machining, slippery liquid-infused surface, tribological properties, asymmetric bump arrays.

1. Introduction

Inspired by the lotus leaf, superhydrophobic surfaces have a very wide range of potential applications in industrial production and daily life, such as self-cleaning, anti-icing, and corrosion resistance [1–5]. However, dry friction occurs when the superhydrophobic surfaces are in contact with solids, which narrows the scope of their application [6]. Different from the gas-liquid-solid three-phase contact between the droplet and the substrate on the superhydrophobic surface, the slippery liquid-infused surface (SLIS) represented by *Nepenthes* [7] can obtain a continuous and chemically homogeneous liquid-liquid contact by pouring various kinds of lubricants into the micro nano structure. When the friction couple contacts, the liquid with very low surface energy on the SLIS transforms the dry friction into oil lubrication friction, to avoid the direct contact of the friction pair. In addition, the microstructure on the SLIS can also store abrasive particles, which can further reduce the surface wear. Therefore, the SLIS can provide an anti-friction guarantee for its practical application in self-cleaning [8], anti-fouling [9–11], anti-icing [12–15], corrosion resistance [16–18], drag reduction [19,20], and water harvesting [21,22].

So far, a great number of methods have been proposed for the fabrication of SLISs. Manna et al. [23] proposed the design of SLIS using nano-porous and chemically reactive polymer multilayers. Yong et al. [24] fabricated a kind of 3D porous network microstructure on polyamide-6 substrate by a femtosecond laser direct writing method. Luo et al. [25] deposited ZnO films onto Si substrates by rf magnetron sputtering to prepare the SLIS, and studied the droplet transportation on the surface under acoustic waves. Chen et al. [26] prepared SLIS on glass and silicon substrates by depositing a polyelectrolyte multilayer film obtained by the layer-by-layer assembly. Although the above methods seem to be effective in

fabricating SLISs, they are only effective for polymers, silicon and glass, but quite powerless for metallic substrates. It is widely known that metallic materials are more widely used in daily life. The effective fabrication of SLISs on metallic substrates fascinated many researchers, and diverse methods have been proposed, such as spraying method [19,27], chemical etching [28,29], electrochemical method [12,22,30], and laser irradiation [31]. In spraying method, the use of easily dispersed organic solvents will cause harm to operators and the environment, and the combination of coating and metallic materials mainly relies on mechanical bonding, resulting in low bonding strength and poor stability with the surface. In the chemical etching and electrochemical processes, a large number of waste strong acid, strong alkali or heavy metal salt solutions will be produced, which can cause great harm to the environment. In addition, chemical etching and electrochemical methods are not suitable for generating arrays with large-scale complex structures. Laser irradiation is a more improved method to obtain large-scale structure arrays on metallic surfaces. However, some dust particles will be produced in the laser irradiation process, which will do some harm to human body and environment. Therefore, developing a green method to satisfy industrial production of slippery liquid-infused metallic surface is in high demand.

Wire electrical discharge machining (WEDM) plays a significant role in the precision manufacturing field. During the process of WEDM, the discharge between the working electrode and the tool electrode produces a plasma channel with high temperature, which causes the materials to be melted and evaporated. Then, these harmful melted materials are flushed away by dielectric fluid, which does not contain strong acid, alkali or heavy metal. Due to its green and precision characteristics, WEDM has been widely used to fabricate microstructural surfaces with special wettability [32–37]. However, the fabrication of

anti-friction slippery liquid-infused metallic surface with sub-millimeter-scale asymmetric bump arrays by WEDM has rarely been reported. In this work, we have developed a simple technique to fabricate SLIS with anti-friction property on various metallic substrates using the WEDM process. The influences of the number of cutting steps on the morphology and wettability of the surface were thoroughly investigated by experiments. In addition, the tribological properties of the fabricated surface were studied by micro-friction and -wear tester, and it was proven that the SLIS had low friction coefficient and slight abrasive wear behavior compared with smooth surface. Of special interest is the fact that slippery sub-millimeter-scale asymmetric bump arrays fabricated by our method showed excellent water harvesting performance at low temperatures, which are expected to have promising application prospects in harsh environments.

2. Experiment

2.1 Materials.

Aluminum alloy (7075), titanium alloy (TC4), stainless steel (304) and brass (H8) were purchased from Shanghai Jiuqin Metal Material Co., Ltd. Ethanol and glycerol were purchased from Beijing Chemical Factory. *1H,1H,2H,2H*-perfluorodecyltriethoxysilane (PFDTES) used to lower surface energy was purchased from Beijing JHYB Pharmaceutical Technology Co., Ltd. Acetone was purchased from Tianjin Xintong Fine Chemical Co., Ltd. Juice, coffee, tea, vinegar, eggs, and ketchup were purchased from a local supermarket. Silicone oil used as the infused lubricant was purchased from Xilong Chemical Co., Ltd. Meilan, congo red, and sudan 3 used as the dyeing agent were purchased from Sinopharm Group Chemical Reagent Co., Ltd.

2.2 Fabrication of SLIS.

The microstructure required by SLIS was processed by a commercially available WEDM. In this process, the electrical processing parameters are shown in Table 1. The offsets of adjacent cutting were 60 μm , 10 μm , and 2 μm , respectively. Molybdenum wire (120 μm in diameter) was loaded as an electrode, and aqueous solution of emulsion was used to enhance the quality of processing. Prior to PFDTES modification, the microstructured surfaces were cleaned with acetone and ethanol and dried naturally, then immersed in a solution consisting of PFDTES and ethanol to lower surface energy for 2 h. To achieve slippery property, the as-obtained surfaces were injected with silicone oil (about 10 $\mu\text{L}/\text{cm}^2$), and subsequently the injected surfaces remained tilted at 30° for a period to ensure that excess silicone oil flowed away from the surfaces. The entire process on the bio-inspired fabrication of SLIS is shown in Fig. 1, and the picture in the upper right in step 3 is *Nepenthes*.

Table 1 Electrical processing parameters.

Order	Wire speed (m/s)	Peak current (A)	Pulse width (μs)	Pulse interval (μs)	Voltage (V)
1 st cut step	11.6	19.2	24	96	100
2 nd cut step	3.9	9.6	6	24	100
3 rd cut step	3.9	5.12	0.4	6	80
4 th cut step	3.9	3.2	0.25	2.5	80

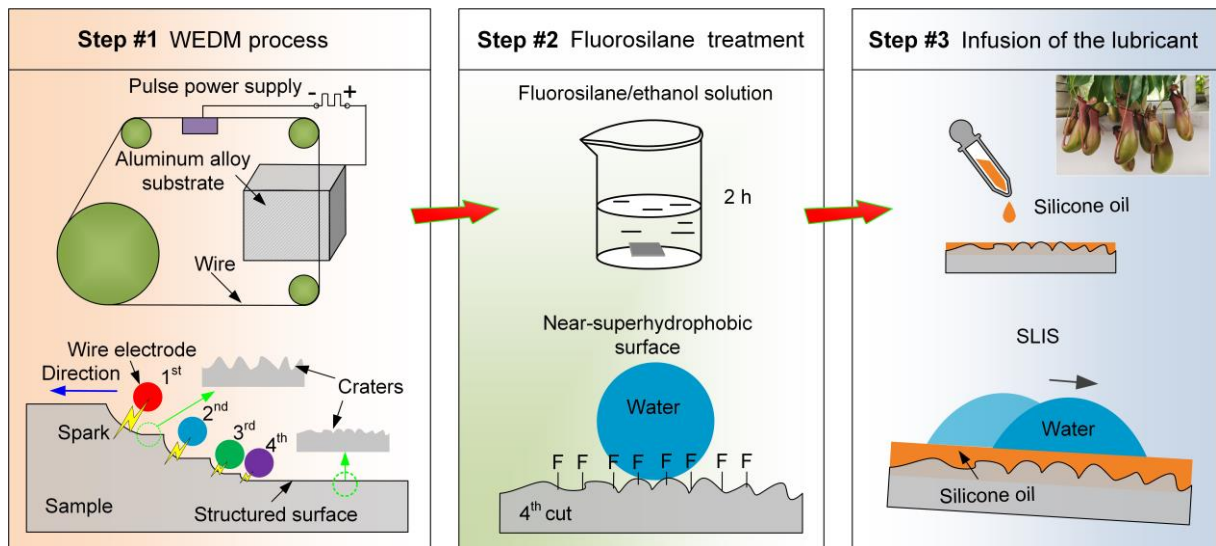


Fig. 1 Schematic diagram of the fabrication process of the SLIS.

2.3 Characterizations.

The morphology of the metallic surfaces was examined by scanning electron microscope (SEM, FEI Quanta 250) and confocal laser scanning microscope (CLSM, ZEISS LSM 700). The roughness (R_a) of the surface was measured using roughness profile measuring instrument (MarSurf LD 120). The chemical composition of the surfaces was analyzed by energy-dispersive X-ray spectroscopy (EDXS, X-max). The wettability of the surfaces was obtained and analyzed using a homemade contact angle meter (JCJ-001). The optical images of the droplets on the surfaces were obtained by digital camera (EOS M3).

2.4 Tribological tests.

The tribological performance of the surfaces was tested using a micro-friction and -wear tester (RETC, MFT-3000). The experimental temperature was 18–20°C, the ambient relative humidity was 45–50%, the load was 0.4 N, the sliding speed was 0.4 mm/s, and the sliding time was 30 min. In the test, a SUS440C steel ball with the diameter of 3.969 mm was used as a mating part, which was composed of 1.10% C, 1.00% Mn, 0.03% P, 0.06% Mo, 0.01% S, 17.5% Cr, 0.60% Ni, 0.50% Cu, 1.00% Si and Fe balance. The reciprocating stroke of the

steel ball on the surfaces was 2 mm.

2.5 Water Harvesting Test.

A humidifier (KZ-HU0001) was used to provide a fog source for the fog collection test (fog flow output: 0.45 L/h). The fog flow with a velocity of 26–31 cm/s was generated by the humidifier, and the diameter of the droplets produced by the humidifier was in the range of 5–15 μm . The water harvesting experiment was performed in a room temperature of 18–20°C and a relative humidity of $23 \pm 2.5\%$, and a refrigeration device was used to cool the samples controlled at -2–1°C. The distance between the humidifier and the sample was about 13 cm, and the sample was fixed in the holder at a 45° inclination angle. Measurements of the water harvesting were recorded three times to average to ensure the correctness of the results.

3. Results and discussion

3.1 Morphology and chemical composition

In the process of WEDM, when the pulse voltage is applied between the sample and the electrode wire, the generated current will break down the working medium to form an electric circuit, which causes a discharge between the electrode wire and the sample, resulting in high temperature spark. Subsequently, the spark triggers the explosion and thermal expansion of the surface of the sample, which takes away the molten material and forms the microstructure [32]. Before the fabrication of microstructure, the formation process of microstructure was numerically simulated by COMSOL multi-physics modelling software. The coupling model of thermal field and flow field of material removal process under single pulse in WEDM was established based on a single discharge point on the electrode wire. It is necessary to make an assumption for the calculation of discharge channel radius $R_p(t)$. According to Kojima [38], the discharge channel will expand rapidly within 2 μs and then remain stable. Therefore, it is

assumed that $R_p(t)$ changes in a linear trend during the expansion time, which is expressed as follows:

$$R_p(t) = \begin{cases} R_S + (R_{\max} - R_S) \cdot \frac{t}{2} & 0 \leq t \leq 2\mu\text{s} \\ R_{\max} & 2\mu\text{s} \leq t \leq t_{on} \end{cases} \quad (1)$$

where R_S is the initial radius of plasma channel, R_{\max} is the radius when the plasma channel reaches equilibrium, and t_{on} is the duration of single pulse discharge.

The distribution of heat flux density $q(r,t)$ in two-dimensional space is expressed as:

$$q(r,t) = \frac{3 \cdot \eta \cdot u_p(t) \cdot I_p(t)}{\pi R_p^2(t)} \cdot \exp\left(-3 \frac{r^2}{R_p^2(t)}\right) \quad (2)$$

The simulation model established in this work is a two-dimensional model, which is divided into two parts: the dielectric region of the discharge gap (size: $10 \times 100 \mu\text{m}$) and the matrix material region before discharge (size: $90 \times 100 \mu\text{m}$). The heat flux with Gaussian distribution is applied to the center of the surface of the base material, and boundary conditions for the model are marked in Fig. 2a.

The governing equations of numerical calculation model of the thermal field and flow field are established as follows:

$$\rho C_p \left(\frac{\partial T}{\partial t} + u \cdot \nabla T \right) = \nabla \cdot (k \nabla T) - Q_{loss} \quad (3)$$

$$\rho \frac{\partial u}{\partial t} + \rho (u \cdot \nabla) u = \nabla \cdot \left[-PI + \mu (\nabla u + \nabla u^T) \right] + \rho g + F_b + F_{st} \quad (4)$$

$$\nabla \cdot u = 0 \quad (5)$$

where ρ is the material density, C_p represents specific heat capacity, T is the temperature, t is the time, k is the thermal conductivity, Q_{loss} is the heat loss, u represents the fluid velocity, P is the flow field pressure, I is the identity matrix, μ is the hydrodynamic viscosity, β is the coefficient of thermal expansion, and F_{st} represents the surface tension. Because these three

equations contain the same variables, the thermal field and flow field are coupled together.

In addition to the electrical parameters shown in Table 1, we also defined other simulation parameters, including the discharge duration t_{on} (10 μ s), discharge stop time t_{off} (10 μ s), initial discharge radius R_s (0.1 μ m) and the anode energy distribution coefficient η (16.7%) [39]. The anode material in the model was set as 7075 Al, and its thermophysical properties are shown in Table 2.

Table 2 Thermophysical properties of 7075Al and interstitial medium [40].

Parameter	Interstitial medium	Anode material (7075Al)
Density (Solid/liquid/gas phase) (kg m^{-3})	-/1000/-	2810/2500/1.3
Thermal conductivity (Solid/liquid/gas phase) ($\text{W m}^{-1}\text{K}^{-1}$)	-/0.59/-	176/85/0.2
Specific heat capacity (Solid/liquid/gas phase) ($\text{J kg}^{-1}\text{K}^{-1}$)	-/4200/-	860.4/1130/-
Dynamic viscosity (Liquid/gas phase) (Pa s)	2.98×10^{-3}	0.005/0.0011
Latent heat of melting (J kg^{-1})	-	3.98×10^5
Latent heat of evaporation (J kg^{-1})	-	1.05×10^7
Melting point (K)	-	901
Boiling point (K)	-	2467
Coefficient of thermal expansion (K^{-1})	-	2.34×10^{-5}

Fig. 2b and 2c shows the temperature distribution and velocity distribution of gasification material during the WEDM process with the different cut steps. For the simulation results of the 1st cut step, the temperature increases gradually under the action of

heat conduction with the increase of time. The melting region can be better observed by extracting the melting point isotherm (901K) of the material at the end of pulse. At the same time, more heat is transmitted to the matrix, resulting in phase transformation [41,42]. The melted material is in the molten pool, and the gasified material quickly escapes from the substrate surface at a certain speed. This effect is more obvious with the action time of the pulse. The simulation results of the 4th cutting process show a similar phenomenon. The difference is that the size of the crater structure became smaller, the heat affected zone formed was reduced, and the movement speed of the gasified material was also slightly reduced.

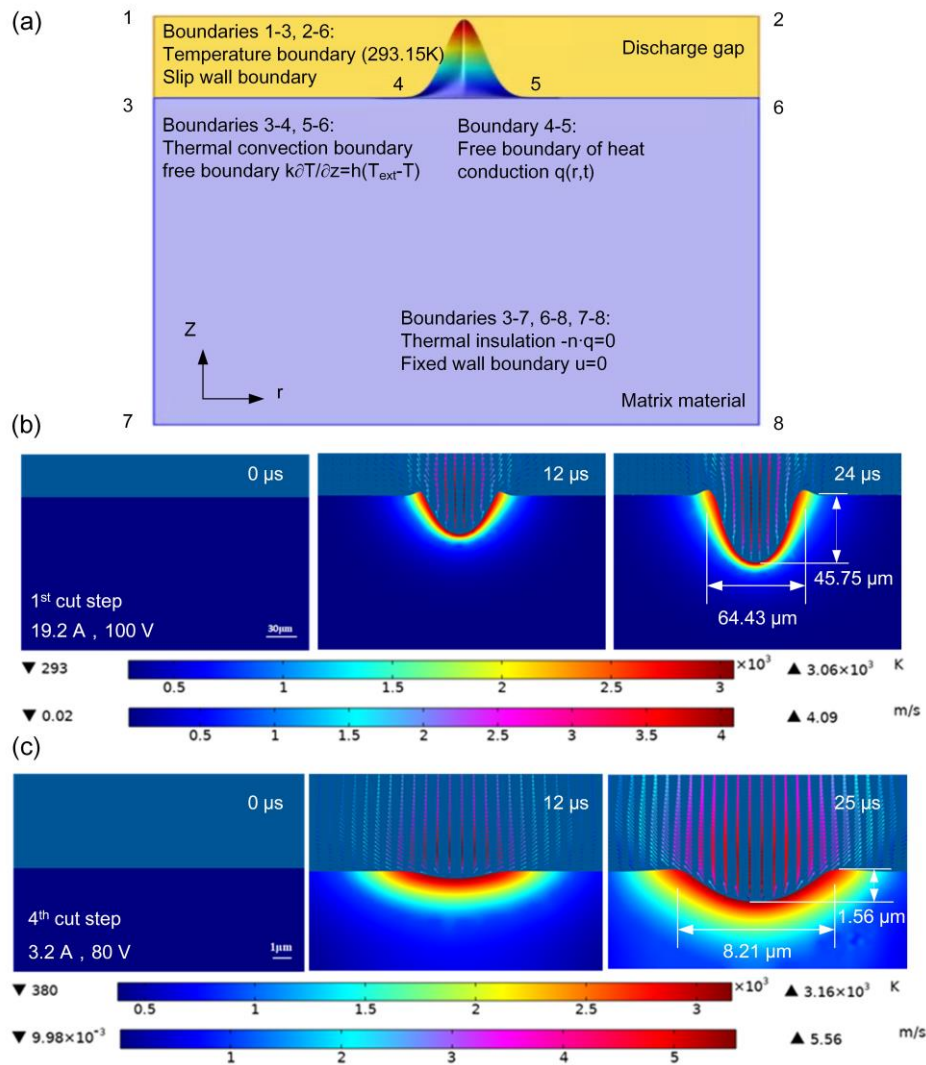


Fig. 2 Numerical simulation of the microstructure fabricated by WEDM. (a) Schematic of the simulation model. (b) and (c) Simulated results to show the temperature distribution and

velocity distribution during the WEDM process with the 1st and 4th cut steps.

To study the effects of the number of cutting steps on the microstructure morphology by experiment, we fabricated four different types of microstructured aluminum alloy surfaces by WEDM from 1st to 4th cut step. Fig. 3 shows the SEM images, CLSM images and surface roughness curves of the different surfaces. In the 1st cut step, the largest electrical discharge energy was used, resulting in the largest size of the crater structure (diameter: 50–80 μm , depth: 15–25 μm) and highest roughness Ra of $5.22 \pm 0.30 \mu\text{m}$ (Fig. 3a). The purpose of the 1st cut step was rough machining, which cut a profile in accordance with the simple programming of wire path. In the 2nd and 3rd cut steps, the applied energy was gradually reduced in such a way that the size of the crater became smaller, and the roughness Ra decreased from $2.02 \pm 0.13 \mu\text{m}$ to $1.01 \pm 0.03 \mu\text{m}$ (Fig. 3b and c). The 2nd and 3rd cut steps were semi-finishing aiming to modify the workpiece size by reasonably setting the offset. In the 4th cut step, the smallest energy was applied obtaining the smallest size of the crater (diameter: 5–15 μm , depth: 1–4 μm) and lowest roughness Ra ($0.78 \pm 0.04 \mu\text{m}$) on the microstructured surface (Fig. 3d). Therefore, the results indicated that the surface became highly smooth after the four cutting steps. In addition, it can be found that the simulation results (Fig. 2b and c) on the diameter of the crater structure of the surfaces fabricated by WEDM with the 1st and 4th cut steps were basically consistent with the experimental results (Fig. 3a and d), but the depth was different for the surface fabricated by WEDM with the 1st cut step. The possible reason is that in the actual process, multiple pulses may overlap when acting on the material, resulting in the difference between the size of the crater structure obtained by the experimental results and the simulation results.

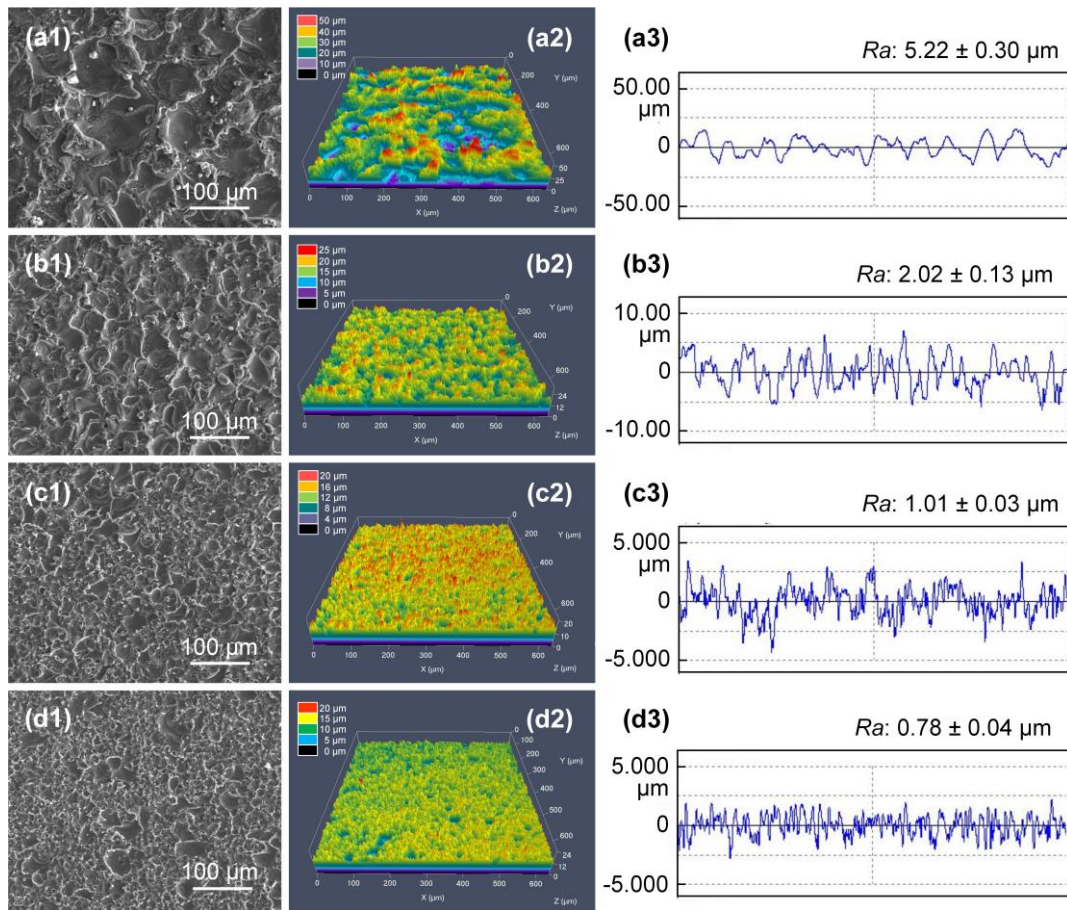


Fig. 3 SEM images, CLSM images and surface roughness curves of the aluminum alloy surfaces fabricated by WEDM with the (a) 1st cut step, (b) 2nd cut step, (c) 3rd cut step, and (d) 4th cut step.

In order to obtain stable slippery property, low surface energy materials need to be used to reduce the surface energy of microstructured surfaces. The variations in chemistry of the fabricated aluminum alloy surface before and after PFDTES modification were investigated using EDXS. Fig. 4a shows the EDXS result of the surface fabricated with the 4th cut step. The result showed that elements C and O were well distributed on the surface. After further PFDTES modification, the element F was observed on the fabricated surface (Fig. 4b).

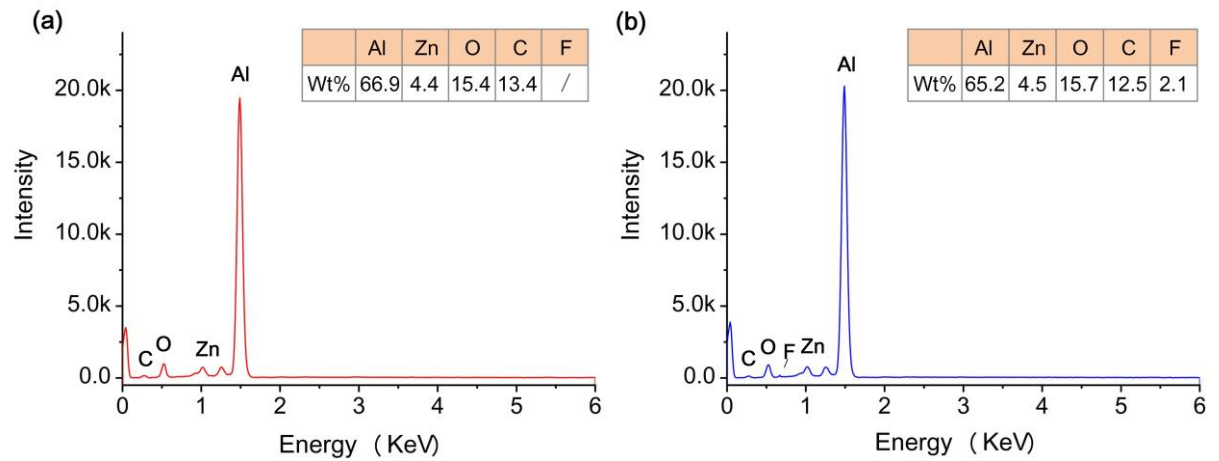


Fig. 4 EDXS results of the fabricated surfaces after the WEDM process with the 4th cut step.

(a) Microstructured surface. (b) Microstructured surface after PFDTES modification.

3.2 Wettability

To achieve an improved water-repellent surface, silicone oil used in the experiment were selected as a model oil phase. Infusion of silicone oil into microstructured aluminum alloy fabricated by WEDM with the 4th cut step yielded stable SLIS with a water contact angle of $116.2 \pm 1.8^\circ$ that allowed droplet (4 μL) of water to slide off unimpededly (Fig. 5a), and the droplet was observed to slide down the surface (tilted at 5°) at the rates of $0.29 \pm 0.02 \text{ mm s}^{-1}$. We have further showed the sliding behavior of a water droplet on the silicone oil-injected smooth surface. As shown in Fig. 5b, the contact angle on the silicone oil-injected smooth surface was $93.8 \pm 2.1^\circ$, and when the surface was turned 90° and 180° , the water droplet adhered to the surface. According to the theory of the SLIS, after the silicone oil penetrated and wet the microstructure (top of step 3 in Fig. 1), the resulting silicone oil film prevented the droplet from directly contacting the surface, resulting in the formation of slippery property (bottom of step 3 in Fig. 1). Therefore, the droplet dropped on the silicone oil-infused surface could perform scroll when the surface was inclined at a certain angle. Fig. 5c shows the time-sequence images of water, juice, coffee, tea, vinegar, albumin, glycerol, and ketchup on

the SLIS. These images revealed that the liquid droplets readily slid down the surface tilted at an angle of 10° without leaving any trace, showing excellent liquid-repellent property.

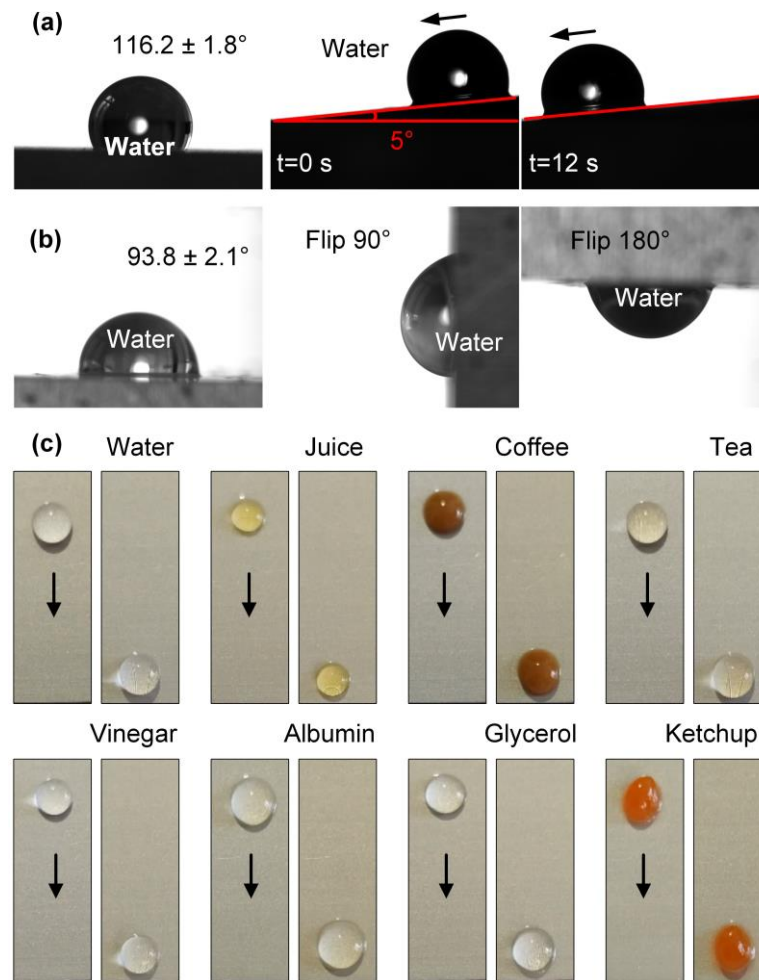


Fig. 5 Wettability of water droplet on different aluminum alloy surfaces. (a) and (b) Contact angle and sliding behavior of SLIS and smooth surface. (c) Images showing various liquids sliding down the fabricated surface.

The change of wettability on the aluminum alloy surfaces fabricated with the different numbers of cut step was studied, as shown in Figure 6. With increasing the number of cut step, the water contact angle on the surface did not change significantly and kept in a range between 116.3° and 118.3° , while the water contact angle hysteresis gradually decreased from $5.8 \pm 1.3^\circ$ to $1.8 \pm 0.4^\circ$ (Fig. 6a). As shown in Fig. 6b, it can be found that the water sliding

angle on the surface also gradually decreased from $7.7 \pm 0.8^\circ$ to $3.1 \pm 1.1^\circ$ as the number of cut step increased. It is considered that an increase in the number of cut step caused the surface to become smoother, and the results for the roughness Ra of different samples are shown in Fig. 3. When the liquid slid on a smoother surface, the resistance that the liquid received became smaller, resulting in the decrease of the sliding angle. Moreover, we compared the sliding angle results with other SLIS on metallic substrates in reported references (Table 3). By comparison, it can be concluded that the sliding angle obtained in our work is close to or even better than that of others. However, the green and precision characteristics for the WEDM technique are much better that can promote the practical applications of SLIS.

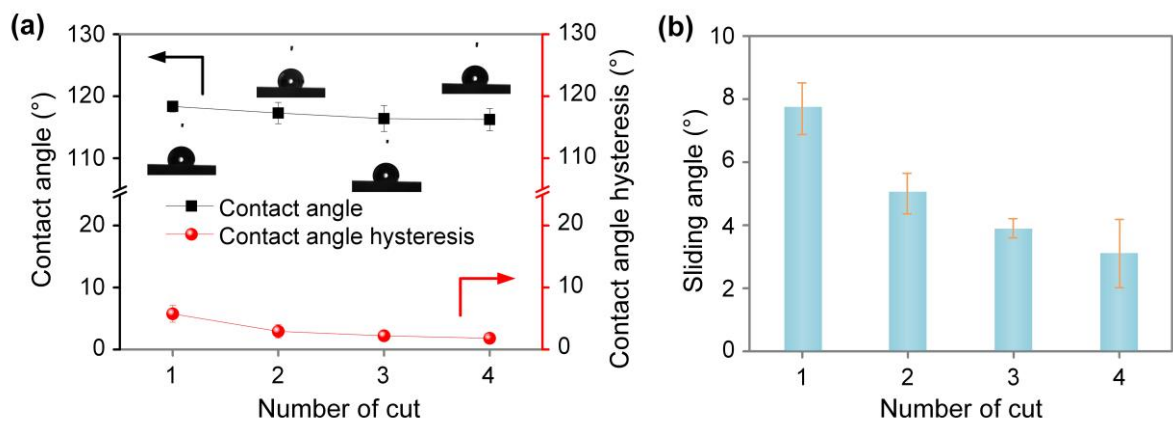


Fig. 6 Changes of (a) contact angle and its hysteresis, and (b) sliding angle on the surfaces fabricated with different numbers of cut step.

Table 3 Comparison with the sliding angle of SLIS in reported references.

Technique	Material	Morphology	Sliding angle	Refs.
Femtosecond laser processing	Stainless steel	Cauliflower-like structure	2°	[43]
Nanosecond laser processing	Carbon steel	Stacked micro/nano structures	2.5°	[44]
Electrochemical etching	Zinc	Needle-like and flake nanostructures	10°	[45]
Electrochemical deposition	Titanium	Dendritic structure	8°	[46]
Hydrothermal method	AZ31 Mg alloy	Nanosheets	7.9°	[47]
Anodic oxidation	Aluminum alloy	Nanoporous structure	5°	[48]
Electrochemical etching and oxidation	Aluminum	Micron-sized stepped structure and nano-sized holes	< 5°	[22]
Electrochemical deposition and anodizing	Cu/Zn alloy	Needle-like structure	11.3°	[49]
Our work	Aluminum alloy	Crater structure	3.1 ± 1.1°	-

3.3 Tribological behaviors

3.3.1 Friction results

During the electrical machining process, a crater structure was formed on the surface of the workpiece material. The presence of such a crater structure can reduce the actual contact area between the two sides of the grinding and determine the friction coefficient of the surface. In addition, the lubricating effect exerted by the lubricant affects the friction behavior of the surface. Therefore, we analyzed the friction behavior of different aluminum alloy surfaces

(smooth surface, silicone oil-injected smooth surface, microstructured surface, and SLIS). Unless otherwise specified, microstructured surface and SLIS refer to the surfaces fabricated by WEDM with the 4th cut step (Fig. 3d).

Fig. 7a shows the friction coefficient curves of smooth surface, silicone oil-injected smooth surface, microstructured surface, and SLIS. The friction coefficients of the two smooth surfaces (smooth surface, silicone oil-injected smooth surface) were significantly higher than those of microstructured surface and SLIS, demonstrating that the microstructures of the surfaces play an important role in reducing the coefficient of friction. The silicone oil-injected smooth surface and SLIS had a lower coefficient of friction than the corresponding surfaces without the injection of silicone oil (smooth and microstructured surfaces), indicating that the injected silicone oil film acted as a friction reducer. Fig. 7b shows the friction coefficient change after 15 friction cycles (each cycle was 10 s). As the sliding time increased (0–140 s), the friction coefficients of the smooth surface kept increasing. However, the microstructured surface and SLIS had a slope for the first 8 s. Then both of the friction coefficients were in their stable stages, indicating that they exhibited significant differences with the smooth surface. The average friction coefficient for different surfaces was compared, as shown in Fig. 7c. The smooth surface had the highest friction coefficient of 0.428 ± 0.02 , while the SLIS fabricated by WEDM with the 4th cut step had the lowest friction coefficient of 0.115 ± 0.01 , reduced by 73.2% compared with the smooth surface. It is worth noting that compared with the surfaces from 2nd to 4th cut step, the friction coefficient of the SLIS after 1st cut step was the largest. This is because the roughness of the SLIS after 1st cut step is too large, so that the shearing effect between the steel ball and the microstructure is significantly enhanced, resulting in an increased friction of the steel ball

being slid on the surface. In addition, a comparison of the friction coefficient of the SLIS developed in our work with that of other reported oil-infused materials has been made in Table 4.

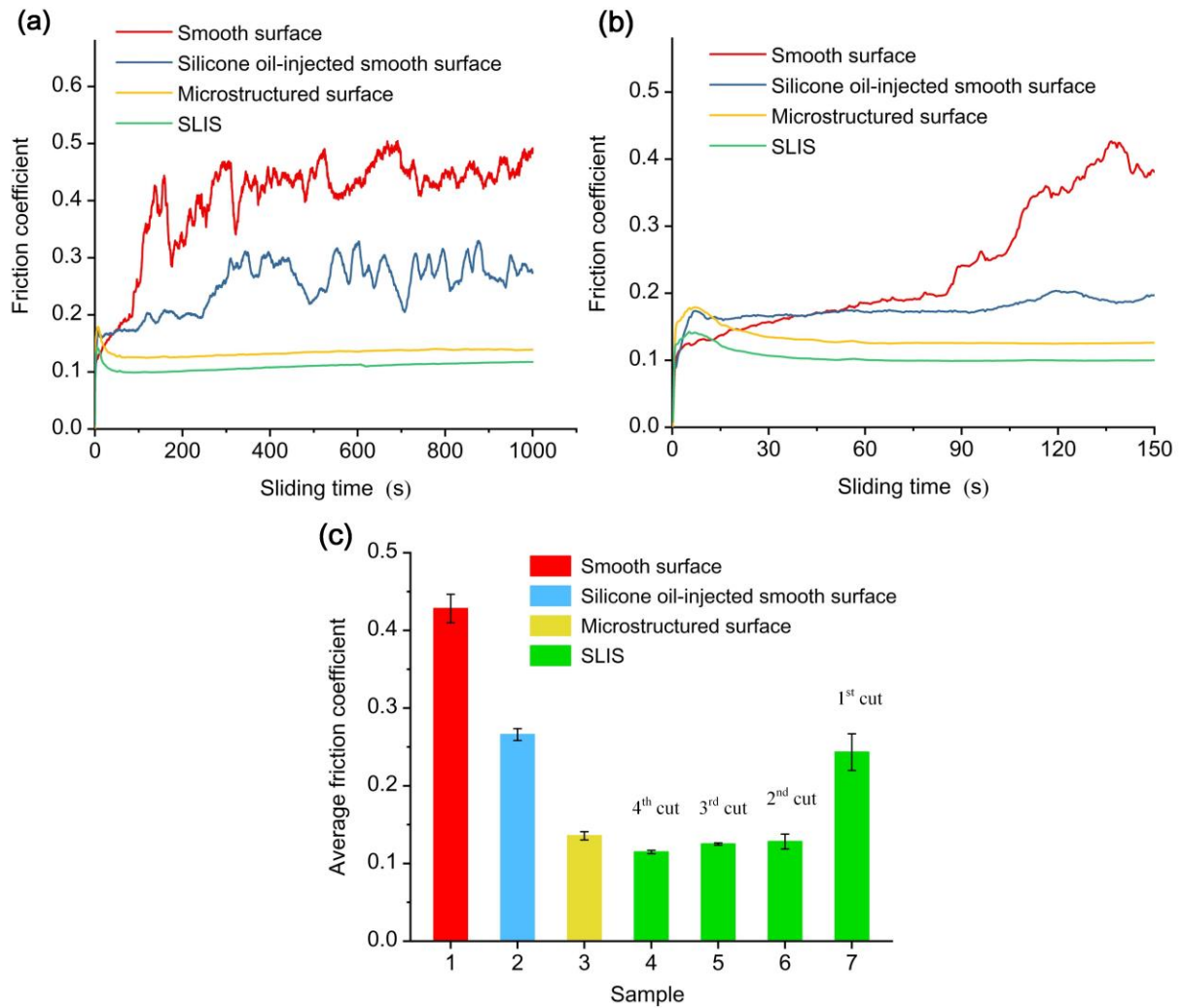


Fig. 7 (a) Friction coefficient curve of smooth surface, silicone oil-injected smooth surface, microstructured surface, and SLIS. (b) Friction coefficient change after 15 friction cycles. (c)

Average friction coefficient of aluminum alloy surfaces under different conditions.

Table 4 Comparison with the previously reported oil-infused materials for friction coefficient.

Technique	Material	Morphology	Infusion	Friction coefficient	Refs.
Electrodeposited method	Ni-Co coating including mesoporous silica nanoparticles	Pinholes and nanoparticles	Silicone oil	0.17	[50]
Shot peening and anodization	Aluminum alloy	Micro-dimples and nano-pores	Krytox GPL 100	0.2	[51]
Nanosecond laser processing	Carbon steel	Stacked micro/nano microstructure	Krytox GPL 105	0.13	[52]
Slip casting process	α -Al ₂ O ₃	Mesoporous structure	Fomblin oil	0.12	[53]
Our work	Aluminum alloy	Crater structure	Silicone oil	0.115	-

3.3.2 Morphology investigations of worn surfaces

The morphology of the worn aluminum alloy surface was studied by scanning electron microscopy and confocal laser scanning microscopy. Fig. 8 indicates the SEM and CLSM images of the wear scar on smooth surface, silicone oil-injected smooth surface, microstructured surface, and SLIS. It is observed in Fig. 8a that the smooth surface had obvious furrow structure and deformation, and wear debris were observed on the wear scar. The form of wear was mainly adhesive wear, and the abrasive wear was also observed. The smooth surface had an obvious wear scar with the width and depth of about 163 μm and 7.85 μm , respectively. As shown in Fig. 8b, although the wear scar width of silicone oil-injected smooth surface was about 175 μm , the wear scar was slight, only showed shallow scratches

(about 2.41 μm), the adhesion and scratching were obviously alleviated and furrow structure was not found. Micrograph of the wear scar on the microstructured surface is shown in Fig. 8c. The wear scar on the surface was relatively slight, only had shallow scratches, and no obvious furrow phenomenon was detected. The reason is that the microstructures on the surface can capture the wear debris generated during the friction process, which significantly improved the wear problem. The microstructured surfaces had the wear scar with a width of about 110 μm . For the SLIS, the wear scar was also relatively slight with only shallow scratches, and the width of the wear scar was reduced to about 88 μm (Fig. 8d). It is further explained that the lubricating property of the silicone oil exhibit a significant wear resistance.

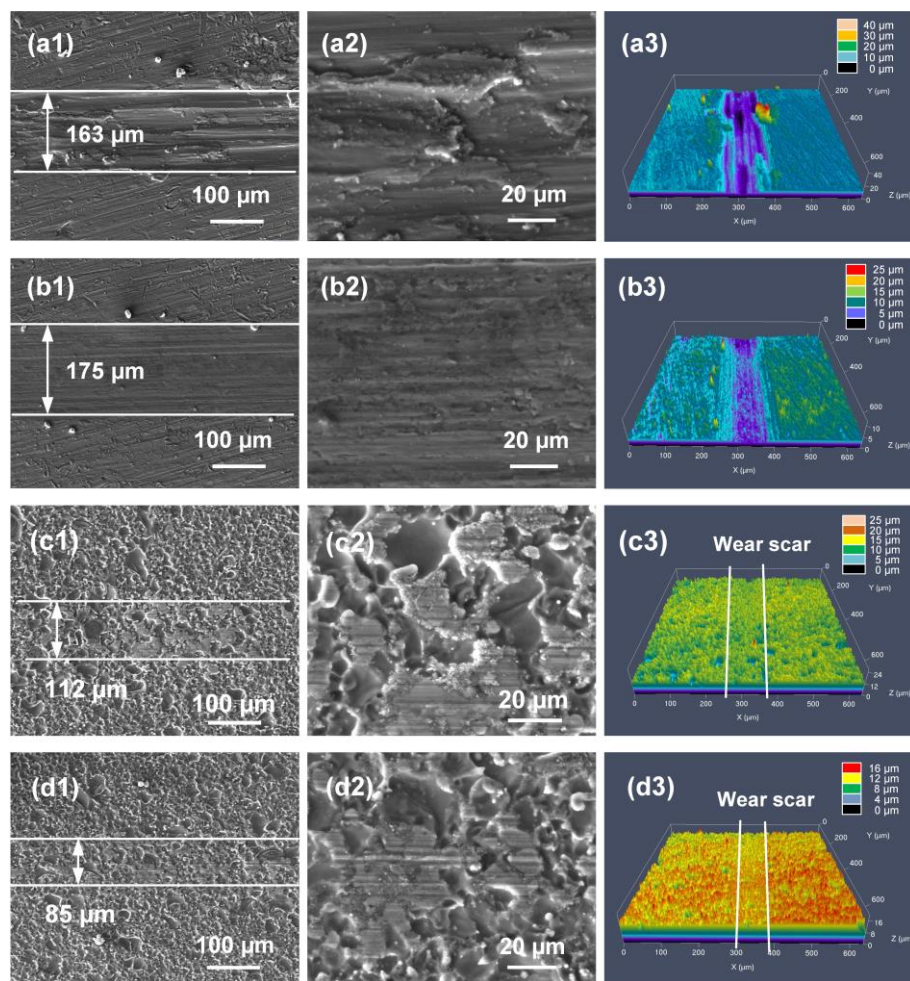


Fig. 8 SEM and CLSM images of the wear scar on (a) smooth surface, (b) silicone oil-injected smooth surface, (c) microstructured surface, and (d) SLIS.

3.3.3 Mechanism analysis

It has been reported that microstructures can significantly affect the friction and wear properties of materials [54,55]. Since a large number of microstructures are distributed on the surface of the material, the microscopic wear mechanism of the material needs to be established when analyzing the wear properties of the material from the microscopic scale. The frictional force can be described by the quantitative parameter friction coefficient (μ). According to the theory proposed by Bowden and Tabor [56], the friction can be decomposed into two parts:

$$\mu = F/W = \mu_a + \mu_p = \frac{A\tau_a + A_p\tau_p}{W} \quad (6)$$

where F is the frictional force, W is the normal load, μ_a is the bonding term (depending mainly on the actual contact area, lubrication conditions and friction pair materials, etc.), μ_p is the plowing term (depending mainly on the degree of elastic deformation), τ is the shearing strength of the material, and A and A_p are the actual contact area and the deformation area between the dual friction materials, respectively.

According to the formula (6), under the condition that the normal load is constant, the friction force is proportional to the actual contact area and the shearing strength. The unprocessed surface is smooth, and has a large contact area with the steel ball, which result in a large friction leading to a high friction coefficient. The microstructured surface, however, has a micro-scale crater structure, helping reduce its actual contact area with the stainless-steel ball significantly, which effectively reduces the adhesion and friction of the material. Furthermore, the crater structure on the surface can capture wear debris, which reduces the contact between the wear debris and the matrix during the friction process,

thereby reducing the abrasive wear [57,58], as shown in Fig. 9a. To provide this evidence, we characterized the worn surface using SEM (Fig. 9b). The result shows that the wear debris were stored in the smaller microstructure. It is worth noting that before the surface is characterized by SEM, the silicone oil on the surface needs to be removed by ultrasonic cleaning to reduce the pollution to the scanning electron microscope equipment. Therefore, wear debris in large crater structure will be cleaned out due to loosening in the process of ultrasonic vibration, while in small crater structure, wear debris is tightly bonded, making it difficult to be cleaned out by ultrasound. Fig. 9c and d shows the EDXS spectra of the wear-free area (map 1) and the wear debris (map 2) in the crater structure. It was seen that there were not only the original elements but also the new elements Si in the map 2, and the contents of Fe, C and O increased. These results indicate that the wear debris were captured by the crater microstructures during the friction process, which results in separation between the debris and the matrix ensuring that the friction and wear of the material surface are reduced.

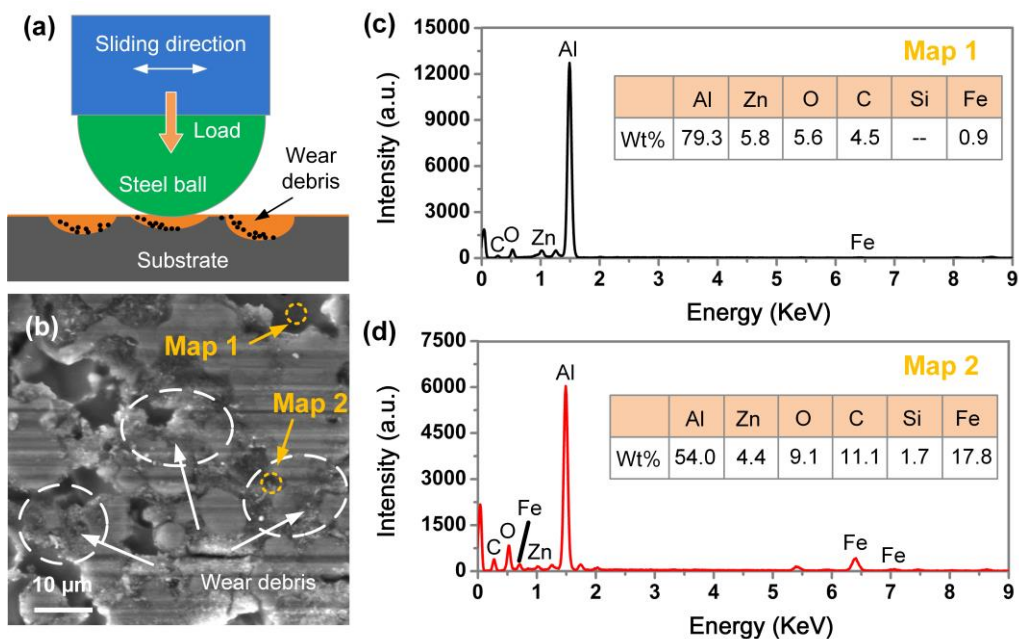


Fig. 9 (a) Model of microstructure capturing wear debris. (b) SEM image of wear debris in

crater structure. (c) EDXS spectra of wear-free crater area (map 1). (d) EDXS spectra of wear debris in the crater structure (map 2).

In addition to the effect of surface microstructures mentioned above, silicone oil film injected onto the surface has a certain antifriction effect, which can be attributed to the lubrication effect of silicone oil [59,60]. The specific heat of silicone oil is large, and the cooling effect on friction heat and the cushioning effect on load are better in friction process. Under the influence of multiple factors such as normal load, friction force, friction heat and material deformation, the long-chain structure of silicone oil molecules will produce a certain degree of polarization, and weak molecular attraction will be generated on the surface of the material to form a physical adsorption film. It is precisely because these adsorbed oil films distribute at the interface of the friction pairs, which acts as a lubrication and antifriction, thus exhibiting the low friction coefficient and wear resistance effect. Besides, the lubricating oil stored in microstructure can provide secondary lubrication to the surface during intervals when lubricant is insufficient ensuring continuous and improved mutual lubrication between the friction pairs [61,62]. In summary, due to the existence of the mechanisms of action of surface microstructure and lubricating oil film, the SLIS shows excellent anti-friction property.

3.4 Applications

The processing range of wire cutting technology is relatively wide, which is not affected by material hardness. Basically, any metallic material can be processed. Fig. 10a–c shows CLSM images of titanium alloy, stainless steel and brass substrates fabricated by WEDM with the 4th cut step. After the WEDM process, there were micro-crater structures on the surfaces of these three metallic substrates with a roughness Ra of $0.51 \pm 0.02 \mu\text{m}$, $0.50 \pm 0.01 \mu\text{m}$, and

$0.94 \pm 0.11 \mu\text{m}$, respectively. After further PFDTES modification and infusion of silicone oil, water droplet on these three samples could roll off easily from the surface tilted at an angle of 10° (Figure 10d–f), showing excellent water-repellent property.

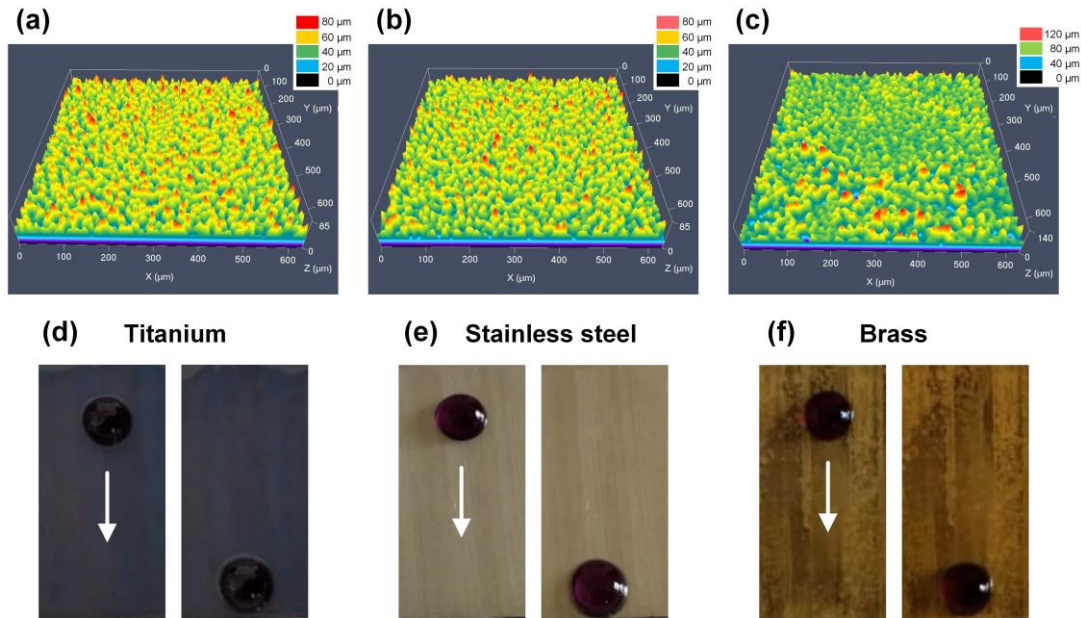


Fig. 10 (a–c) CLSM images and (d–f) water-repellent property of titanium alloy, stainless steel and brass substrates fabricated by WEDM.

In addition, in the process of WEDM, the machining path and position can be precisely controlled by computer through simple programming. Therefore, the surface with complex structure based on SLIS can be designed and manufactured by WEDM. Recently, Park et al. [21] developed slippery asymmetric bumps shown in Fig. 11a for efficient water harvesting at room temperature, but the preparation process involved two processing methods, including template method and boiling water treatment. Here, we presented a simple process to fabricate sub-millimeter-scale asymmetric bump arrays on aluminum alloy substrate by using WEDM with the 4th cut step, and evaluated the water harvesting capacity of the surface at low temperature, which will enrich the application environment of asymmetric bump arrays. Fig. 11a illustrates a schematic of the WEDM process for fabricating sub-millimeter-scale

asymmetric bump arrays. As seen from Fig. 11b and c, the fabricated surface shows regular and visible sub-millimeter-scale asymmetric bump arrays with the front to rear and left to right spacings of 7.50 mm and 4.75 mm, respectively. On the substrate, the large area asymmetric bump arrays will provide a fast and effective water collection capacity.

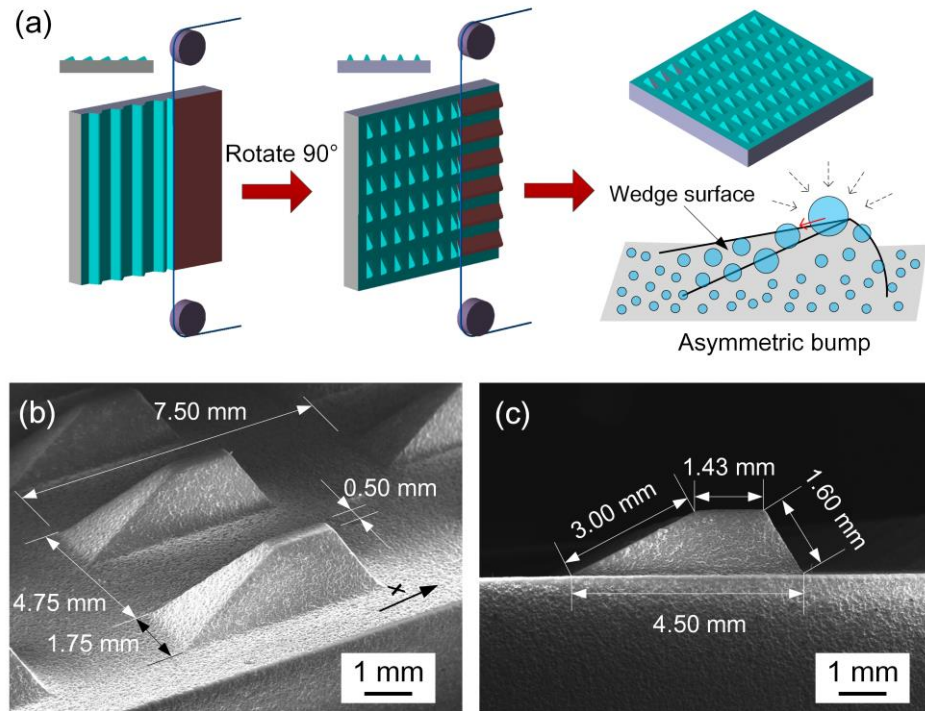


Fig. 11 (a) Fabrication process of sub-millimeter-scale asymmetric bump. (b) and (c)

Stereoscopic images of asymmetric bump arrays.

To demonstrate the water harvesting behavior of the surface at low temperature, we need to further treat the surface with PFDTES modification and infusion of silicone oil to obtain the slippery property. As shown in Fig. 12, when the slippery asymmetric bump arrays were exposed to the fog, small water droplets quickly adhere to the surface. With the growth of the droplets, coalescence occurred between water droplets. Due to the slippery property of the asymmetric bump arrays, the coalesced water droplets could be easily removed from the surface under the action of gravity.

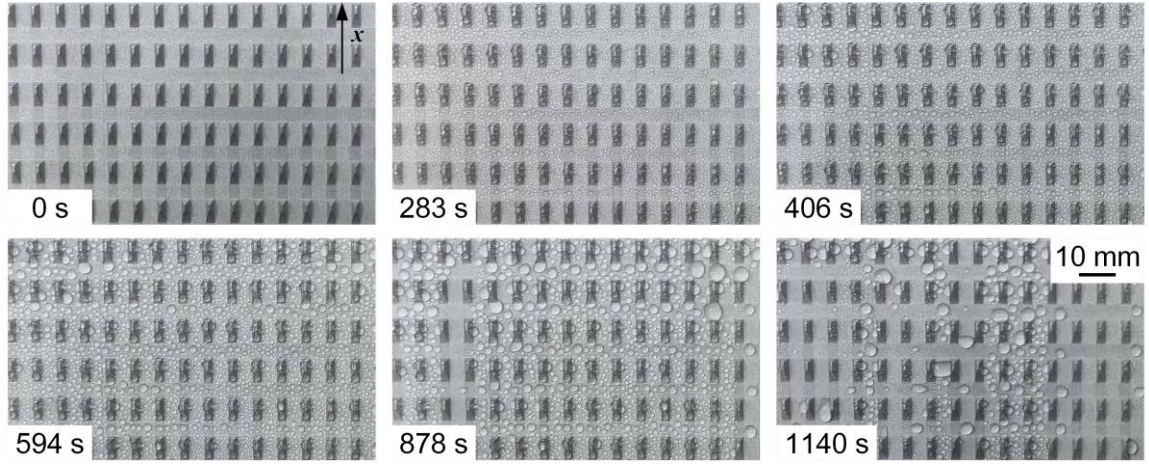


Fig. 12 Water harvesting process on the slippery asymmetric bump arrays in foggy atmosphere.

In order to comprehensively evaluate the water harvesting performance of slippery asymmetric bump arrays, we compared and analyzed the water harvesting behavior of different surfaces. Fig. 13a shows the weight of water collected from different samples within 30 minutes. Surprisingly, the water collection on the smooth surface was 0 g. By observing the water harvesting behavior on the smooth surface, we found that small water droplets will gradually freeze during the growth process on the surface (Fig. 13b). However, the water droplets on the SLIS did not freeze before the water droplets grew, slipped away, and collected, as shown in Fig. 13c. The main reason for this is that the oil film on the SLIS affected the heat transfer between the surface and droplets. The heat transfer between the solid surface and the droplet can be described as

$$\Phi = kA\Delta T \quad (7)$$

where Φ is the heat transfer, k is the thermal conductivity, A is the contact area, and ΔT is the temperature difference between the solid surface and the droplet. The oil film formed on the SLIS reduced the thermal conductivity, thus reducing the heat transfer, so that the water droplets would not freeze on the surface.

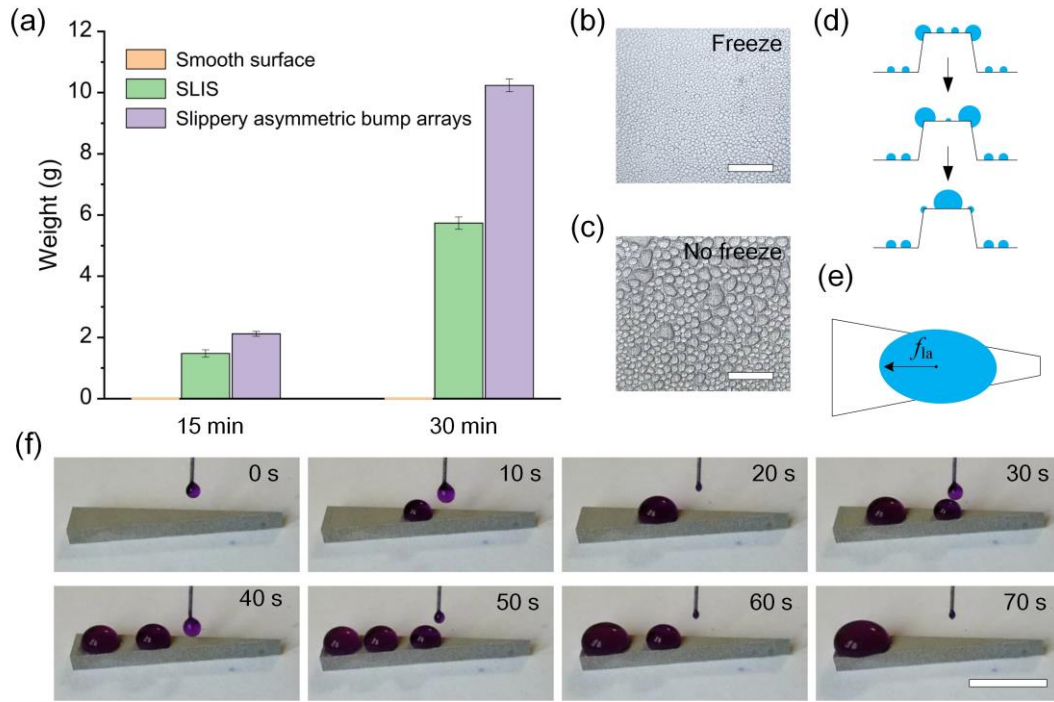


Fig. 13 Water harvesting performance and theory of different surfaces. (a) Weight of water collected from different samples. Condensation property of (b) smooth surface and (c) SLIS on a cooling device at a temperature of $-2\text{--}1^{\circ}\text{C}$. (d) Schematic diagram growth behavior at the top of the asymmetric bump array. (e) and (f) Movement of water droplet driven by Laplace pressure on a wedge surface. The scale bar is 10 mm.

Besides, for both surfaces with slippery characteristics, it can be found that the weight of water collection from slippery asymmetric bump arrays was 10.2 g, which was 78.9% higher than that of the SLIS without asymmetric bump structure. The asymmetric bump arrays have a dual advantage in water harvesting application. One is that water droplets can grow rapidly at the top of the asymmetric bump array [21], as shown in Fig. 13d. The other is that the combination of the slippery performance and the wedge surface on the asymmetric bump array can quickly separate the condensed droplets from the surface. Due to the slippery performance of the surface, the resistance received during the droplet sliding process will be reduced. At the same time, the movement of water droplet on a wedge surface from the

narrow zone to the wide zone will be driven by Laplace force (f_{la}) [22,63,64], as shown in Fig. 13e. In order to verify this theory, we fabricated a wedge-shaped surface and demonstrated the movement of droplets on the surface under the action of Laplace force. When the droplet was placed in a narrow zone of the wedge surface, the droplet was driven by the Laplace force, and then contacted and merged with the previously distributed droplet. When two droplets merged, the driving force increased, and the surface energy was converted into kinetic energy, so that the merged droplets continue to move (Fig. 13f). In this case, water droplets on asymmetric bump arrays are expected to quickly leave the surface. Therefore, these results show that the slippery asymmetric bump arrays fabricated by our technology has excellent water collection performance at low temperature.

4. Conclusions

In summary, we fabricated bio-inspired SLIS by WEDM technique, and the micro-crater structure was simply distributed on various metallic substrates by the WEDM process. After further PFDTES modification and infusion of silicone oil, the as-obtained surfaces showed excellent liquid-repellent property. Various liquids including water, juice, coffee, tea, vinegar, albumin, glycerol, and ketchup could easily slide down the SLIS when it was tilted at an angle of 10° . Next the tribological properties of SLIS were studied in detail. The SLIS fabricated by WEDM with the 4th cut had the lowest friction coefficient of 0.115 ± 0.01 , representing a decrease of 73.2% in friction coefficient as compared to that of the smooth surface. The width and depth of wear scar on SLIS reduced significantly compared with that of the smooth surface. More important, slippery asymmetric bump arrays fabricated by WEDM has great potential to be applied for water collection at low temperatures. It is reasonable, therefore, to

conclude that this research can provide an effective and green strategy for the fabrication of functional materials with large scale complex structure.

Acknowledgments

This work was supported by the National Natural Science Foundation of China (No. U19A20103), the China Postdoctoral Science Foundation (No. 2019M661184), and the Jilin Province Scientific and Technological Development Program (No. YDZJ202101ZYTS025).

Compliance with ethical standards

Conflict of interest The authors declare that they have no conflicts of interest.

References

- [1] Liu, M. J., Wang, S. T., & Jiang, L. (2017). Nature-inspired superwettability systems. *Nature Reviews Materials*, 2, 17036.
- [2] Si, Y. F., Dong, Z. C., & Jiang, L. (2018). Bioinspired designs of superhydrophobic and superhydrophilic materials. *ACS Central Science*, 4, 1102–1112.
- [3] Kreder, M. J., Alvarenga, J., Kim, P., & Aizenberg, J. (2016). Design of anti-icing surfaces: smooth, textured or slippery? *Nature Reviews Materials*, 1, 15003.
- [4] Kang, B., Sung, J., & So, H. (2021). Realization of superhydrophobic surfaces based on three-dimensional printing technology. *International Journal of Precision Engineering and Manufacturing-Green Technology*, 8, 47–55.
- [5] Barthwal, S., & Lim, S. H. (2020). Robust and chemically stable superhydrophobic aluminum-alloy surface with enhanced corrosion-resistance properties. *International Journal of Precision Engineering and Manufacturing-Green Technology*, 7, 481–492.
- [6] Jung, K. K., Jung, Y., Park, B. G., Choi, C. J., & Ko, J. S. (2021) Super wear resistant nanostructured superhydrophobic surface. *International Journal of Precision Engineering and Manufacturing-Green Technology*. Doi: 10.1007/s40684-021-00325-8.
- [7] Wong, T. S., Kang, S. H., Tang, S. K. Y., Smythe, E. J., Hatton, B. D., Grinthal, A., & Aizenberg, J. (2011). Bioinspired self-repairing slippery surfaces with pressure-stable omniphobicity. *Nature*, 477, 443–447.
- [8] Wu, X. H., & Chen, Z. (2018). A mechanically robust transparent coating for anti-icing

and self-cleaning applications. *Journal of Materials Chemistry A*, 6, 16043–16052.

- [9] Epstein, A. K., Wong, T. S., Belisle, R. A., Boggs, E. M., & Aizenberg, J. (2012). Liquid-infused structured surfaces with exceptional anti-biofouling performance. *Proceedings of the National Academy of Sciences of the United States of America*, 109, 13182–13187.
- [10] Zhou, X., Lee, Y. Y., Chong, K. S. L., & He, C. B. (2018). Superhydrophobic and slippery liquid-infused porous surfaces formed by the self-assembly of a hybrid ABC triblock copolymer and their antifouling performance. *Journal of Materials Chemistry B*, 6, 440–448.
- [11] Xiao, L. L., Li, J. S., Mieszkin, S., Di Fino, A., Clare, A. S., Callow, M. E., Callow, J. A., Grunze, M., Rosenhahn, A., & Levkin, P. A. (2013). Slippery liquid-infused porous surfaces showing marine antibiofouling properties. *ACS Applied Materials & Interfaces*, 5, 10074–10080.
- [12] Kim, P., Wong, T. S., Alvarenga, J., Kreder, M. J., Adorno-Martinez, W. E., & Aizenberg, J. (2012). Liquid-infused nanostructured surfaces with extreme anti-ice and anti-frost performance. *ACS Nano*, 6, 6569–6577.
- [13] Wilson, P. W., Lu, W. Z., Xu, H. J., Kim, P., Kreder, M. J., Alvarenga, J., & Aizenberg, J. (2013). Inhibition of ice nucleation by slippery liquid-infused porous surfaces (SLIPS). *Physical Chemistry Chemical Physics*, 15, 581–585.
- [14] Juuti, P., Haapanen, J., Stenroos, C., Niemela-Anttonen, H., Harra, J., Koivuluoto, H., Teisala, H., Lahti, J., Tuominen, M., Kuusipalo, J., Vuoristo, P., & Makela, J. M. (2017). Achieving a slippery, liquid-infused porous surface with anti-icing properties by direct deposition of flame synthesized aerosol nanoparticles on a thermally fragile substrate. *Applied Physics Letters*, 110, 161603.
- [15] Zhang, J. L., Gu, C. D., & Tu, J. P. (2017). Robust slippery coating with superior corrosion resistance and anti-icing performance for AZ31B Mg alloy protection. *ACS Applied Materials & Interfaces*, 9, 11247–11257.
- [16] Tuo, Y. J., Zhang, H. F., Chen, W. P., & Liu, X. W. (2017). Corrosion protection application of slippery liquid-infused porous surface based on aluminum foil. *Applied Surface Science*, 423, 365–374.
- [17] Wang, P., Lu, Z., & Zhang, D. (2015). Slippery liquid-infused porous surfaces fabricated on aluminum as a barrier to corrosion induced by sulfate reducing bacteria. *Corrosion Science*, 93, 159–166.
- [18] Qiu, R., Zhang, Q., Wang, P., Jiang, L. N., Hou, J., Guo, W. M., & Zhang, H. X. (2014). Fabrication of slippery liquid-infused porous surface based on carbon fiber with enhanced

corrosion inhibition property. *Colloids and Surfaces A: Physicochemical and Engineering Aspects*, 453, 132–141.

- [19] Wang, Y., Zhang, H. F., Liu, X. W., & Zhou, Z. P. (2016). Slippery liquid-infused substrates: a versatile preparation, unique anti-wetting and drag-reduction effect on water. *Journal of Materials Chemistry A*, 4, 2524–2529.
- [20] Hemeda, A. A., & Tafreshi, H. V. (2016). Liquid-infused surfaces with trapped air (LISTA) for drag force reduction. *Langmuir*, 32, 2955–2962.
- [21] Park, K. C., Kim, P., Grinthal, A., He, N., Fox, D., Weaver, J. C., & Aizenberg, J. (2016). Condensation on slippery asymmetric bumps. *Nature*, 531, 78–82.
- [22] Luo, H., Lu, Y., Yin, S. H., Huang, S., Song, J. L., Chen, F. Z., Chen, F. J., Carmalt, C. J., & Parkin, I. P. (2018). Robust platform for water harvesting and directional transport. *Journal of Materials Chemistry A*, 6, 5635–5643.
- [23] Manna, U., & Lynn, D. M. (2015). Fabrication of liquid-infused surfaces using reactive polymer multilayers: Principles for manipulating the behaviors and mobilities of aqueous fluids on slippery liquid interfaces. *Advanced Materials*, 27, 3007–3012.
- [24] Yong, J. L., Chen, F., Yang, Q., Fang, Y., Huo, J. L., Zhang, J. Z., & Hou, X. (2017). Nepenthes inspired design of self-repairing omniphobic slippery liquid infused porous surface (SLIPS) by femtosecond laser direct writing. *Advanced Materials Interfaces*, 4, 1700552.
- [25] Luo, J. T. T., Geraldi, N. R. R., Guan, J. H. H., Mchale, G., Wells, G. G. G., & Fu, Y. Q. Q. (2017). Slippery liquid-infused porous surfaces and droplet transportation by surface acoustic waves. *Physical Review Applied*, 7, 014017.
- [26] Chen, X. C., Ren, K. F., Wang, J., Lei, W. X., & Ji, J. (2017). Infusing lubricant onto erasable microstructured surfaces toward guided sliding of liquid droplets. *ACS Applied Materials & Interfaces*, 9, 1959–1967.
- [27] Wang, N., Xiong, D. S., Lu, Y., Pan, S., Wang, K., Deng, Y. L., & Shi, Y. (2016). Design and fabrication of the lyophobic slippery surface and its application in anti-icing. *The Journal of Physical Chemistry C*, 120, 11054–11059.
- [28] Gao, X. Y., & Guo, Z. G. (2017). Mechanical stability, corrosion resistance of superhydrophobic steel and repairable durability of its slippery surface. *Journal of Colloid and Interface Science*, 512, 239–248.
- [29] Wang, N., Xiong, D. S., Pan, S., Deng, Y. L., & Shi, Y. (2016). Fabrication of superhydrophobic and lyophobic slippery surface on steel substrate. *Applied Surface Science*, 387, 1219–1224.

- [30] Wang, P., Zhang, D., Lu, Z., & Sun, S. M. (2016). Fabrication of slippery lubricant-infused porous surface for inhibition of microbially influenced corrosion. *ACS Applied Materials & Interfaces*, 8, 1120–1127.
- [31] Doll, K., Fadeeva, E., Schaeske, J., Ehmke, T., Winkel, A., Heisterkamp, A., Chichkov, B. N., Stiesch, M., & Stumpp, N. S. (2017). Development of laser-structured liquid-infused titanium with strong biofilm-repellent properties. *ACS Applied Materials & Interfaces*, 9, 9359–9368.
- [32] Bae, W. G., Song, K. Y., Rahmawan, Y., Chu, C. N., Kim, D., Chung do, K., & Suh, K. Y. (2012). One-step process for superhydrophobic metallic surfaces by wire electrical discharge machining. *ACS Applied Materials & Interfaces*, 4, 3685–3691.
- [33] Liu, Y., Moevius, L., Xu, X., Qian, T., Yeomans, J. M., & Wang, Z. (2014). Pancake bouncing on superhydrophobic surfaces. *Nature Physics*, 10, 515–519.
- [34] Liu, C., Liu, Q., Jin, R., Lin, Z., & Xu, Y. (2020). Mechanism analysis and durability evaluation of anti-icing property of superhydrophobic surface. *International Journal of Heat and Mass Transfer*, 156, 119768.
- [35] Zhou, C. L., Wu, X. Y., Lu, Y. J., Wu, W., Zhao, H., & Li, L. J. (2018). Fabrication of hydrophobic Ti₃SiC₂ surface with micro-grooved structures by wire electrical discharge machining. *Ceramics International*, 44, 18227–18234.
- [36] Wang, H., Chi, G., Wang, Y., Yu, F., & Wang, Z. (2019). Fabrication of superhydrophobic metallic surface on the electrical discharge machining basement. *Applied Surface Science*, 478, 110–118.
- [37] Chen, Z., Yan, Z., Zhou, H., Han, F., & Yan, H. (2021). One-step fabrication of the wear-resistant superhydrophobic structure on SiCp/Al composite surface by WEDM. *Surface & Coatings Technology*, 409, 126876.
- [38] Kojima, A., Natsu, W., & Kunieda, M. (2008). Spectroscopic measurement of arc plasma diameter in EDM. *CIRP Annals-Manufacturing Technology*, 57, 203-207.
- [39] Pérez, R., Carron, J., Rappaz, M., Walder, G., Revaz, B., & Flukiger, R. (2007). Measurement and metallurgical modelling of the thermal impact of EDM discharges on steel. *Proceedings of the 15th International Symposium on Electromachining*, 17-22.
- [40] Wang, Y., Yao, S. W., Ding, Z. J., Wu, C. Z., & Xiong, W. (2021). Machining characteristics of USV-MF complex assisted WEDM-LS based on multi-physical coupling. *International Journal of Precision Engineering and Manufacturing-Green Technology*, 8, 387–404.
- [41] Salvati, E., & Korsunsky, A. M. (2020). Micro-scale measurement & FEM modelling of

residual stresses in AA6082-T6 Al alloy generated by wire EDM cutting. *Journal of Materials Processing Technology*, 275, 116373.

- [42] Tang, J. J., & Yang, X. D. (2018). Simulation investigation of thermal phase transformation and residual stress in single pulse EDM of Ti-6Al-4V. *Journal of Physics D-Applied Physics*, 51, 135308.
- [43] Zouaghi, S., Six, T., Bellayer, S., Moradi, S., Hatzikiriakos, S. G., Dargent, T., Thomy, V., Coffinier, Y., Andre, C., Delaplace, G., & Jimenez, M. (2017). Antifouling biomimetic liquid-infused stainless steel: application to dairy industrial processing. *ACS Applied Materials & Interfaces*, 9, 26565–26573.
- [44] Ma, Q., Wang, W., & Dong, G. N. (2019). Facile fabrication of biomimetic liquid-infused slippery surface on carbon steel and its self-cleaning, anti-corrosion, anti-frosting and tribological properties. *Colloids and Surfaces A-Physicochemical and Engineering Aspects*, 577, 17–26.
- [45] Luo, H., Yin, S. H., Huang, S., Chen, F. J., Tang, Q. C., & Li, X. J. (2019). Fabrication of slippery Zn surface with improved water-impellent, condensation and anti-icing properties. *Applied Surface Science*, 470, 1139–1147.
- [46] Ouyang, Y. B., Zhao, J., Qiu, R., Hu, S. G., Chen, M., & Wang, P. (2019). Liquid-infused superhydrophobic dendritic silver matrix: a bio-inspired strategy to prohibit biofouling on titanium. *Surface & Coatings Technology*, 367, 148–155.
- [47] Yao, W. H., Chen, Y. H., Wu, L., Zhang, J. K., & Pan, F. S. (2022). Effective corrosion and wear protection of slippery liquid-infused porous surface on AZ31 Mg alloy. *Surface & Coatings Technology*, 429, 127953.
- [48] Yang, Z. C., He, X. Y., Chang, J. F., Bai, X. Q., Cao, P., & Yuan, C. Q. (2021). Fabrication of biomimetic slippery liquid-infused porous surface on 5086 aluminum alloy with excellent antifouling performance. *Surface and Interface Analysis*, 53, 147–155.
- [49] Qiu, Z. H., Qiu, R., Xiao, Y. M., Zheng, J. Y., & Lin, C. G. (2018). Slippery liquid-infused porous surface fabricated on CuZn: a barrier to abiotic seawater corrosion and microbiologically induced corrosion. *Applied Surface Science*, 457, 468–476.
- [50] Bai, S. F., Liu, X. H., Xu, L. K., Xuan, J. J., Liu, Y. R., Shao, Y., Xin, Y. L., Li, X. B., & Fan, L. (2022). Enhancement of corrosion resistance and lubricating performance of electrodeposited Ni-Co coating composited with mesoporous silica nanoparticles and silicone oil impregnation. *Materials Chemistry and Physics*, 282, 125929.
- [51] Jambor, M., Kajaneck, D., Fintova, S., Broncek, J., Hadzima, B., Guagliano, M., & Bagherifard, S. (2021). Directing surface functions by inducing ordered and irregular morphologies at single and two-tiered length scales. *Advanced Engineering Materials*, 23,

2001057.

- [52] Ma, Q., Wang, W., & Dong, G. N. (2019). Facile fabrication of biomimetic liquid-infused slippery surface on carbon steel and its self-cleaning, anti-corrosion, anti-frosting and tribological properties. *Colloids and Surfaces A-Physicochemical and Engineering Aspects*, 577, 17–26.
- [53] Rowthu, S., & Hoffmann, P. (2018). Perfluoropolyether impregnated mesoporous alumina composites overcome the dewetting-tribological properties trade-off. *ACS Applied Materials & Interfaces*, 10, 10560–10570.
- [54] Wakuda, M., Yamauchi, Y., Kanzaki, S., & Yasuda, Y. (2003). Effect of surface texturing on friction reduction between ceramic and steel materials under lubricated sliding contact. *Wear*, 254, 356–363.
- [55] Chen, F. Y., Ying, J. M., Wang, Y. F., Du, S. Y., Liu, Z. P., & Huang, Q. (2016). Effects of graphene content on the microstructure and properties of copper matrix composites. *Carbon*, 96, 836–842.
- [56] Bowden, F. P., & Tabor, D. (2001). *The friction and lubrication of solids*, London: Oxford University Press.
- [57] Fan, H. Z., Zhang, Y. S., Hu, T. C., Song, J. J., Ding, Q., & Hu, L. T. (2015). Surface composition-lubrication design of Al₂O₃/Ni laminated composites—Part I: Tribological synergy effect of micro-dimpled texture and diamond-like carbon films in a water environment. *Tribology International*, 85, 142–151.
- [58] Golchin, A., Wikner, A., & Emami, N. (2016). An investigation into tribological behaviour of multi-walled carbon nanotube/graphene oxide reinforced UHMWPE in water lubricated contacts. *Tribology International*, 95, 156–161.
- [59] Tang, J. Z., Ding, Q., Zhang, S. W., & Hu, L. T. (2016). The fracture mechanism and the corresponding optimization strategy for nonhydrogenated amorphous carbon film in dimethyl silicone oil. *Surface & Coatings Technology*, 307, 941–950.
- [60] Quan, X., Hu, M., Gao, X. M., Fu, Y. L., Weng, L. J., Wang, D. S., Jiang, D., & Sun, J. Y. (2016). Friction and wear performance of dual lubrication systems combining WS₂-MoS₂ composite film and low volatility oils under vacuum condition. *Tribology International*, 99, 57–66.
- [61] Andersson, P., Koskinen, J., Varjus, S. E., Gerbig, Y., Haefke, H., Georgiou, S., Zhmud, B., & Buss, W. (2007). Microlubrication effect by laser-textured steel surfaces. *Wear*, 262, 369–379.
- [62] Huang, W., Jiang, L., Zhou, C. X., & Wang, X. L. (2012). The lubricant retaining effect of

micro-dimples on the sliding surface of PDMS. *Tribology International*, 52, 87–93.

- [63] Cao, M., Yu, C., Xiao, X., Zhang, B., Zhang, Y., Zhang, C., Ma, H., Cui, X., Li, Z., & Jiang, L. (2018). Bioinspired pressure-tolerant asymmetric slippery surface for continuous self-transport of gas bubbles in aqueous environment. *ACS Nano*, 12, 2048–2055.
- [64] Ghosh, A., Ganguly, R., Schutzius, T. M., & Megaridis, C. M. (2014). Wettability patterning for high-rate, pumpless fluid transport on open, non-planar microfluidic platforms. *Lab on a Chip*, 14, 1538–1550.